

Strain Engineering of Quantum emitters in Hexagonal Boron Nitride

Noah Mendelson, Milos Toth, Igor Aharonovich,^{*} and Toan Trong Tran^{*}

School of Mathematical and Physical Sciences, University of Technology Sydney, Ultimo, New South Wales 2007, Australia.

^{*} Corresponding author: igor.aharonovich@uts.edu.au; trongtoan.tran@uts.edu.au

Abstract: Quantum emitters in hexagonal boron nitride (hBN) are promising building blocks for the realization of integrated quantum photonic systems. However, spectral inhomogeneity of the sources limits their potential applications. Here, we apply tensile strain to quantum emitters embedded in few-layer hBN films and realize both red and blue spectral shifts with tuning magnitudes up to 65 meV, a record for any quantum source in a solid-state system. We demonstrate reversible tuning of the emission and discuss the results in the framework of electron-phonon coupling. Additionally, evidence for the modification of spin orbit-coupling between excited and meta-stable states, and rotation of the emission dipole upon straining is presented and discussed. Our work demonstrates the potential for the strain tuning of quantum emitters in layered materials for their employment in scalable quantum photonic networks.

Single photon emitters (SPEs) embedded in solid state hosts are a critical building block for a range of quantum technologies.¹⁻³ Integrating multiple SPEs with on-chip nanophotonic components provides a scalable route towards the engineering of quantum gates and quantum circuitry.⁴⁻⁶ However, unwanted interactions between the atom-like defects and the crystal host environment lead to spectral inhomogeneity that hinders device performance. To address this issue, methods for tuning emitter properties are critical for generating identical photons,⁷⁻⁹ and for coupling to high-quality factor photonic resonators where tuning magnitudes must be comparable to or greater than the cavity linewidths.¹⁰

Recently, hexagonal boron nitride (hBN), has been shown to host a range of sub-band gap defects operating as room temperature SPEs.¹¹⁻¹⁴ These SPEs display a number of desirable properties, including high photon purity,¹⁵ bright emission,¹⁶ and favorable quantum efficiencies.¹⁷ However, the emitters have been shown to be susceptible to environmental influences, which lead to extreme inhomogeneity in their emission properties,¹⁸ including a broad, continuous spectral range of zero phonon lines spanning from the deep ultraviolet to the near infrared.¹⁹⁻²¹ Consequently, reliable tuning methods for controlling the emission properties are paramount for their implementation in quantum photonic applications.

Initial reports on tuning of hBN emitters employed voltage-controlled Stark shift devices and hydrostatic pressure.²²⁻²⁵ Strain-based tuning of hBN defects has also been investigated using either the application of surface acoustic waves,^{26, 27} or mechanical deflection of solid beams that translated vertical displacements to horizontal strain tensors.²⁸ In this work, we employ high degrees of tensile strain to tune the emission of hBN SPEs, and achieve record tuning magnitudes of up to 20 nm (65meV). Unlike all previous reports, we take advantage of large area (\sim few mm²) ultrathin hBN films (\sim < 10 nm) that host a variety of SPEs.²⁹⁻³² These samples are amenable to the direct application of tensile strain (as is detailed below), and we report both red and blue

spectral shifts, relating our results to the local density of phonon states. Recent calculations predicted strain-induced modification of defect-phonon coupling, which we realize for the first time experimentally.³³ Additionally, we observe reversible changes to the optical properties of the studied SPEs, therefore offering a promising route to deterministically tailor light-matter interactions in these systems.

Strain experiments were performed on hBN films grown by chemical vapor deposition (CVD) on a copper foil to a thickness of ~ 7 nm.²⁹ The films were transferred from the copper foil using a polymer-assisted (PMMA) wet-transfer process to a PDMS slab of 2.7 cm in length, and ~ 200 μ m thick (*cf. methods*). The hBN/PDMS slab was secured in a mechanical straining device and mounted for optical characterization *via* confocal microscopy, as shown in Figure 1a. The PDMS slab was subject to varying degrees of tensile strain, as shown schematically in Figure 1b. Throughout the manuscript, we will discuss the strain applied to the PDMS substrate to interpret the corresponding results, expressed as the strain percentage (S), defined as $S(\%) = \frac{\Delta L}{L} * 100$, where L is the original length of the PDMS slab, and ΔL is the applied displacement. This provides an upper bound on the strain applied to the hBN film. The precise magnitude is not known as the strain transfer efficiency from PDMS to hBN is unresolved, additionally depending on the layer number where the defect resides, as discussed in the supplementary materials. Incomplete strain transfer likely accounts for the finding that S values of up to 7.4% did not destroy the hBN film.

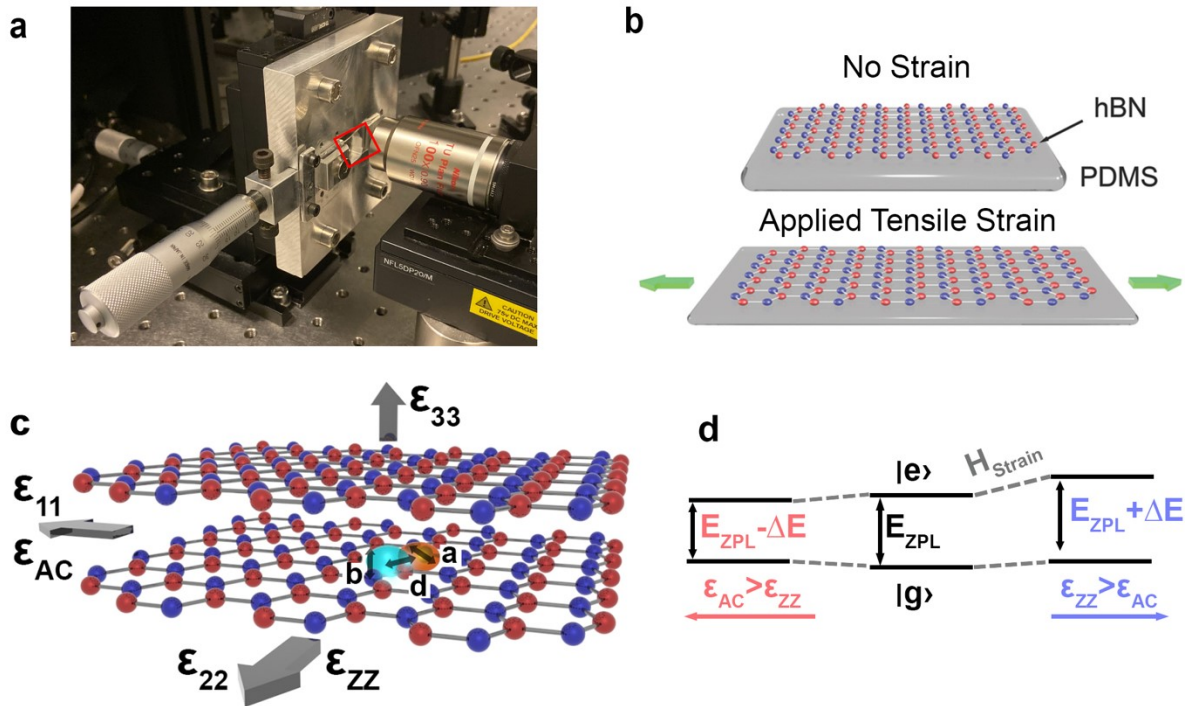


Figure 1. Experimental setup and strain-induced blue shift of 13nm. *a.* Apparatus used to perform the strain tuning experiments. The red box highlights the PDMS slab with a ~ 7 nm hBN film on top. *b.* Schematic showing the application of tensile strain to the PDMS slab. *c.* Schematic illustration of hBN film displaying a defect wavefunction and the strain tensors ϵ_{11} , ϵ_{22} , ϵ_{33} . The electron and hole are characterized by “a” in-plane localization, “b” out-of plane localization, and “d” the separation distance. The strain tensors are depicted as follows, ϵ_{11} corresponds to in-

plane strain along the arm-chair axis (ϵ_{AC}), ϵ_{22} to in-plane strain along the zig-zag axis (ϵ_{ZZ}), and ϵ_{33} to the inter-layer strain contribution. **d.** A simplified model showing the ground ($|g\rangle$) and excited state ($|e\rangle$) state levels for an atomic defect in hBN. When tensile strain is applied, H_{strain} , the energy levels of the defect are modified changing the emission energy of the defect ZPL by $\pm \Delta E$.

Figure 1c depicts a simplified illustration of an atomic defect that acts as an SPE in hBN. The in-plane and out-of-plane localization lengths a and b , charge separation d , and the deformation potentials of the electron and hole D_e and D_h dictate the line shape and the phonon coupling dynamics of the defect.³⁴ A strain field causes displacement of the lattice sites, distorting the symmetry of the defect wavefunction, and changing its relationship with the surrounding phonon bath. This can be approximated by $H_{\text{strain}} = \sum_{ij} \sigma_{ij} \epsilon_{ij}$, where σ_{ij} are the orbital operators and ϵ_{ij} represent the relevant strain tensors. Three strain tensors must be considered, two describing in-plane components (ϵ_{11} , ϵ_{22}), and one the out-of-plane component (ϵ_{33}) along the c axis of the material. For hBN, the in-plane strain tensors ϵ_{11} and ϵ_{22} are oriented along the arm-chair and zig-zag axes of the crystal, respectively, and will be referred to as ϵ_{AC} and ϵ_{ZZ} .

Emitters in hBN have been reported to exhibit a range of complex dependencies on the applied strain. For example, high-pressure measurements in which strain is applied isotropically have been interpreted in terms of a competition between the inter- and intra-layer strain tensors.²² This, however, is not relevant to our experiment, where tensile strain is applied predominantly along the intralayer axis of hBN, meaning that the in-plane strain tensors will dominate the resulting optical response. The response of emitters to in-plane strain has been investigated by simulations of defect complexes of the type X-V, where X represents B, N, or heteroatom impurities, and V is a vacancy.²⁸ While the structural nature of the emitters remains unclear, recent simulations have confirmed X-V defects such as $N_B V_N$ and $C_B V_N$ are likely candidates.³⁵⁻³⁷ The simulations suggest that the orientation of the defect dipole relative to the direction of applied strain ϵ_{AC} or ϵ_{ZZ} determines the direction of the ZPL shift for a given defect.²⁸ Two zig-zag ($ZZ_{1\&2}$) and arm-chair ($AC_{1\&2}$) axes exist, each with different effects on the direction of the shift, however, the following discussion is simplified to discuss only relative contributions of strain along the ZZ_1 and AC_1 axes. Specifically, when $\epsilon_{AC} > \epsilon_{ZZ}$ a red shift is observed, while in the case where $\epsilon_{AC} < \epsilon_{ZZ}$ an increase in emission energy occurs (blue shift).²⁸ This is depicted in Figure 1d by a simplified electron energy diagram with an initial ground state $|g\rangle$ and excited state $|e\rangle$ of the defect, and the application of a strain field H_{strain} which modifies the positions of the energy levels according to the relative magnitudes of ϵ_{AC} and ϵ_{ZZ} . Other relevant parameters are discussed in the supporting information.

We use the above framework, summarized in Figure 1, to explore the effects of tensile strain on the optical properties of SPEs in CVD-grown thin films of hBN. Figure 2a shows an SPE at 0% strain (red trace), with an initial ZPL position at 573.40 ± 0.08 nm, and an FWHM of 21.9 ± 0.8 nm. The inset is the corresponding second-order autocorrelation function, $g^2(\tau)$, confirming that the emitter is an SPE ($g^2(0) < 0.5$). Upon application of 3.70% strain, the peak blue shifts to 560.82 ± 0.05 nm, a shift of ~ 12.6 nm (~ 49 meV). The increased emission energy suggests strain is applied primarily along zig-zag axis $\epsilon_{ZZ} > \epsilon_{AC}$. Solid traces in Figure 2a display the Lorentzian fits for the ZPL at each position, and the extracted FWHMs are shown in Figure 2b. We observe a significant decrease in the broadening of the ZPL which narrows from 21.9 ± 0.8 nm to 11.7 ± 0.5 nm after the shift. This decrease (~ 9.0 nm) represents a nearly two-fold reduction in the coupling between the defect and available phonon modes, as will be discussed in detail later.

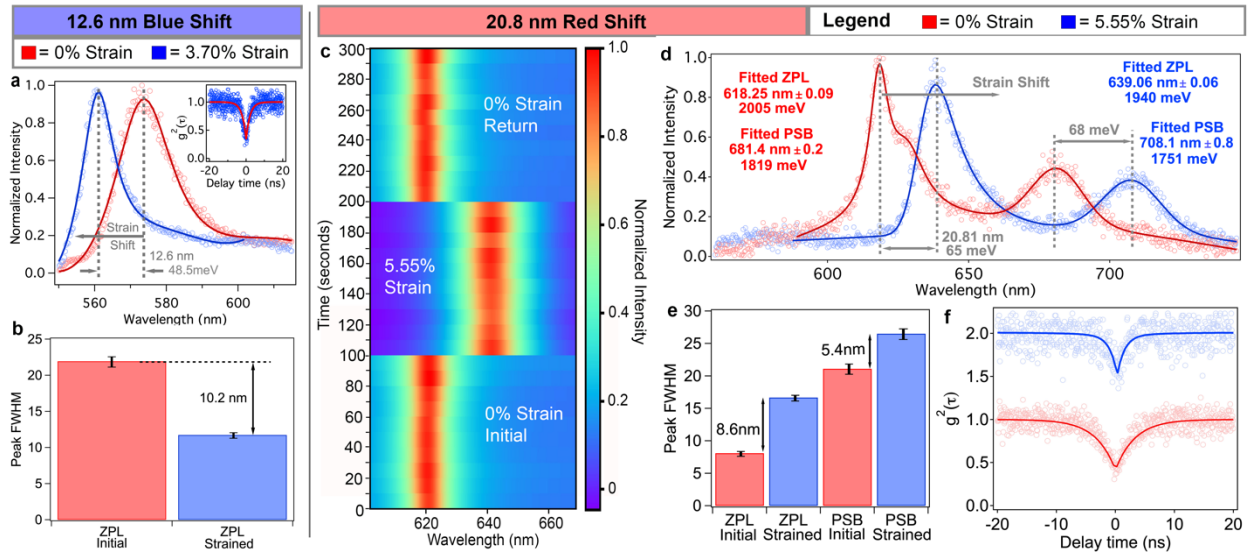


Figure 2. Large red and blue strain-induced shifts. In a-b, d-e red corresponds to initial SPEs while blue corresponds to shifted emission lines. **a.** A tensile strain of 3.70% is applied to an SPE initially at 573.40 ± 0.08 nm (red trace), inducing a blue shift of ~ 12.6 nm to 560.82 ± 0.04 nm (blue trace). Raw data for each (circles) is fitted with Lorentzian functions shown as a solid trace. Inset displays the $g^2(\tau)$ function confirming the quantum nature of the emission at 0% strain. **b.** The FWHM of both peaks are plotted showing a ~ 9.0 nm decrease in the associated linewidth of the emitter from 21.9 ± 0.8 nm (0% strain) to 12.9 ± 0.5 nm (3.7% strain). **c.** A time-resolved spectral acquisition for an SPE at 0% strain (bottom), 5.55% strain (middle), and returning to 0% strain (top). Each panel displays ten consecutive spectral acquisitions of 10 seconds each, demonstrating negligible spectral diffusion during the measurement, and the reversibility of the strain-induced red shift. There is a time offset between the three measurements, and each is normalized individually. **d.** Spectrum of the SPE at 0% strain (red trace) with a ZPL centered at 618.25 ± 0.09 nm, and at 5.55% strain (blue trace) with a ZPL centered at 639.06 ± 0.06 nm, showing a red shift of ~ 20.8 nm or ~ 65.0 meV. Raw data for each (circles) is fitted with Lorentzian functions shown as a solid trace. See figure S2 regarding shoulder peak in 0% strain spectra. **e.** A bar graph plotting the FWHM of the ZPL and the PSB peaks at 0% and 5.55% strain, respectively. Both the ZPL and PSB experience a significant increase in the homogeneous broadening upon straining. **f.** The $g^2(\tau)$ collection for the unstrained and strained SPE, showing a decrease of ~ 2.5 ns for the extracted excited state lifetime of the emitter upon straining.

Next, we investigate the observed shift of a second SPE upon applying tensile strain. Figure 2c shows PL spectra acquired *versus* time before straining (bottom panel), after the application of 5.55% strain (middle panel), and once the strain field is released (top panel). We observe a large and reversible red shift, and optical stability during the 100-second acquisition steps. The $g^2(\tau)$ and spectrum for each collection step are shown in figure S1. The fitted SPE peaks before (618.25 ± 0.09 nm) and after applying 5.55% strain (639.06 ± 0.06 nm) are plotted in figure 2d and demonstrate a red shift of ~ 20.8 nm (~ 65 meV). This constitutes the largest tuning magnitude for any solid-state SPE to date. It is noted that the shoulder peak apparent in the unstrained emission peak is due to the fluorescence signal from PDMS (Figure S2). The red shift suggests strain is applied primarily along the arm-chair axis, $\epsilon_{AC} > \epsilon_{ZZ}$. Alignment between the defect dipole and the applied field, for both strain and Stark based tuning, also influences the magnitude of the observed

energy shift according to equation S1. The large shift magnitude for this particular SPE suggests that the degree of misalignment between the strain field and the defect dipole is small and was indeed confirmed to be only $\sim 10^\circ$, figure S3.

Figure 2e plots the extracted FWHM of the ZPL and PSB before (red) and after (blue) applying 5.55% strain, where a broadening of 8.6 nm and 5.4 nm, respectively, are observed. For the ZPL peak this more than doubles the peak width from 8.1 ± 0.3 nm to 16.7 ± 0.4 nm, an increase of 106%, while the changes to the PSB are less prominent representing a FWHM increase of 25.5% from 21.1 ± 0.6 nm to 26.5 ± 0.8 nm. Recent work has attributed ZPL broadening in hBN to the coupling of the defect with both low-energy longitudinal acoustic (LA) phonon modes as well as local mode oscillations which describe atomic displacements of the defect in relation to the host crystal.³⁴ Conversely, changes in the FWHM of the PSB can be attributed to a modification of coupling strength to longitudinal optical (LO) phonon modes LO_1 and LO_2 ,³⁴ which are responsible for the prominent PSB typically observed ~ 160 meV red-shifted from the ZPL.²¹ While the change in coupling to any one mode cannot be extracted, it is clear that the strain-induced coupling changes vary for different phonon modes.

The red-shift induced increase in phonon coupling lies in stark contrast to the decrease in phonon coupling found for the blue-shift in Figure 2a. In-fact all strain shifted SPEs follow this relationship between changes to the homogeneous broadening of the ZPL and PSB and the direction of the shift observed. Blue shifts decrease the prevalence of phonon coupling, while red-shifts increase the phonon coupling. The dependence of relative phonon coupling to the shift direction is attributed primarily to changes in the deformation potentials of the electron and hole. Where an increase in energy for $|D_e - D_h|$ leads to increased coupling to LA modes, and a lesser extent LO phonon modes, precisely as previously predicted.³⁴ Conversely, as the relationship $|D_e - D_h|$ decreases in energy, coupling to phonon modes becomes less prevalent. An increasing homogeneous broadening accompanying red-shifts has also been observed for stark shifts of hBN emitters,²⁹ but has not previously been explained. Interestingly, we also observe a reversible decrease in the fluorescence lifetime for this SPE, Figure 2f and Figure S1, consistent with the mixing of excited states through electron-phonon coupling processes.^{7, 38}

We now turn our attention to the photophysical modifications of the emission upon applying strain. To this extent, we analyze the polarization of the emitter and record its photon statistics at each step. Figure 3 (a – d) shows the results of increasing tensile strain, at the values of 0% (red), 1.85% (green), 3.70% (light blue), and 5.55% (royal blue), where individual fits are displayed in figure S4. The red shifted ZPL peak moves 2.4 nm (6 meV) at 5.5% strain, figure 3a. The $g^2(\tau)$ measurement at each strain value is shown in figure S5, demonstrating the quantum nature of the emission, and showing no changes to the SPE purity upon straining. Consistent with investigations of higher energy defects (<690 nm), the red shift for this emitter is accompanied by a gradual broadening of the ZPL peak, suggesting increasing coupling to phonon modes, Figure 3b. Figure 3c displays the emission dipole angle as a function of the applied strain, showing a clear rotation upon straining. The dipole angle at 0% strain is $\sim 155^\circ$, and gradually rotates with increasing strain to a value of $\sim 143^\circ$ at 5.55%, a $\sim 12^\circ$ rotation, moving towards the applied strain field at 90° (270°). Note, the hBN film is not rotated relative to the PDMS substrate, as evidenced by the confocal maps at each strain value (figure S6). As a result, we attribute the observed dipole rotation to a distortion of the excited state orbital symmetry, rotating gradually towards the strain field as the strain increases. To the best of our knowledge this is the first demonstration of a strain-induced dipole rotation for a room-temperature SPE and is predominantly possible due to the 2D nature of the host crystal.^{39, 40}

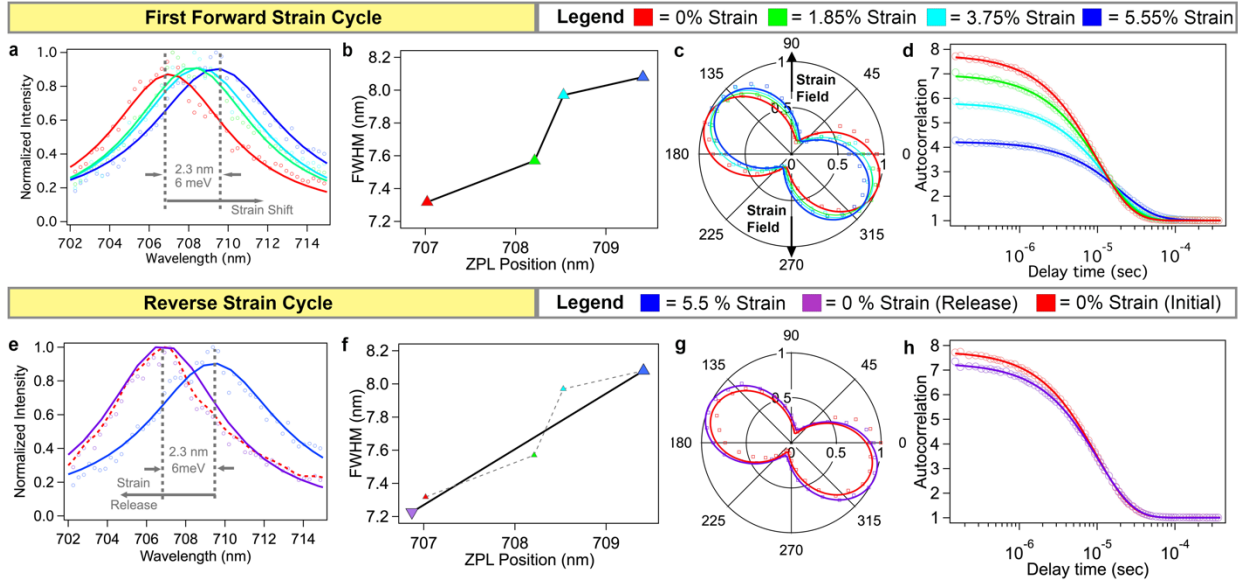


Figure 3. Strain tuning the photophysical properties of hBN SPEs. The first row (a-d) displays a gradual increase in tensile strain from 0% to 5.55%. The second row (e-h) displays the reversing the strain from 5.55% back to 0%. The legend for both rows displays the strain percentage for a corresponding color. **a.** A gradual ZPL red shift of ~ 2.4 nm (~ 6 meV) is observed for increasing strain values. Each collection is fit with Lorentzian functions (solid trace). **b.** The extracted ZPL FWHM vs position with increasing strain, displaying a gradual increase mirroring the observed spectral shift. **c.** Emission dipole orientation of the SPE with increasing strain. The tensile strain field is applied along the 90° (270°) axis, depicted with two arrows. A gradual rotation of the dipole to a maximum displacement of $\sim 12^\circ$ is observed. **d.** Extended autocorrelation measurements for each strain %, fit with a double exponential function, suggesting the presence of two metastable states. The probability of transition into available meta-stable states is cut roughly in half at the maximum applied strain. **e.** Reversibility of the 2.4 nm red shift, while the red dashed line shows the initial spectrum for reference. Each collection is fit with Lorentzian functions (solid trace). **f.** The extracted ZPL FWHM vs position, displaying reversibility of the homogeneous broadening. Data points from the initial forward strain cycle are plotted in the background. **g.** Emission dipole orientation returns to its original position. **h.** Extended autocorrelation measurements, again fitted with a double exponential function, demonstrate the relative bunching is restored to initial values.

Figure 3d displays the second-order auto-correlation measurements for the SPE as a function of applied strain. A significant decrease in photon bunching is observed as the strain field increases. Each curve is fitted with a double exponential, implying contributions from two available metastable states, according to equation S3. The degree of photon bunching observed is known to depend on the excitation power of the system,⁴¹ as the population of the meta-stable state increases with the relative population of the excited state. In the current experiment, however, identical excitation conditions were used at each strain value. The transition from the excited to the meta-stable state requires an intersystem crossing event,⁴² and as such, the probability of this event upon excitation (K_{23}) is controlled by the degree of spin-orbit coupling between the levels (see figure S7 for simplified level structure). The decrease in bunching upon increasing strain suggests that the magnitude of spin-orbit coupling is gradually reduced. A decrease in bunching

was observed for all strained emitters, irrespective of the shift magnitude or direction, for example see Figure S3.

We next explore the reversibility of the strain-induced changes for the same SPE. Figure 3e shows the ZPL position is restored to its initial position (dashed red) upon releasing the applied strain (purple). Similarly, we find that the FWHM of the peak (Figure 3f), the dipole orientation (figure 3g), and the relative bunching (Figure 3h), are also restored to their initial values. Critically, this rules out the potential for layer slippage or permanent damage to the hBN lattice, such as ripping, confirming the strain-induced nature of the effects. Figure S8 displays a second forward strain cycle to higher maximum strain value of 7.40%, showing a larger red shift (~ 4.7 nm) and enhanced changes to the phonon coupling, dipole rotation, and meta-stable state occupation rates.

Finally, we turn our attention to the overall trends observed across all investigated hBN SPEs. Figure 4a displays the relative change in the FWHM *versus* the shift magnitude and direction. Each circle represents a different SPE. In all recorded examples, the trend of ZPL narrowing with blue shifts and broadening with red shifts is conserved. At low shift magnitudes, the changes to the relative electron-phonon coupling appear to change faster, while the shift to peak width ratio changes drops off slightly for larger shift values.

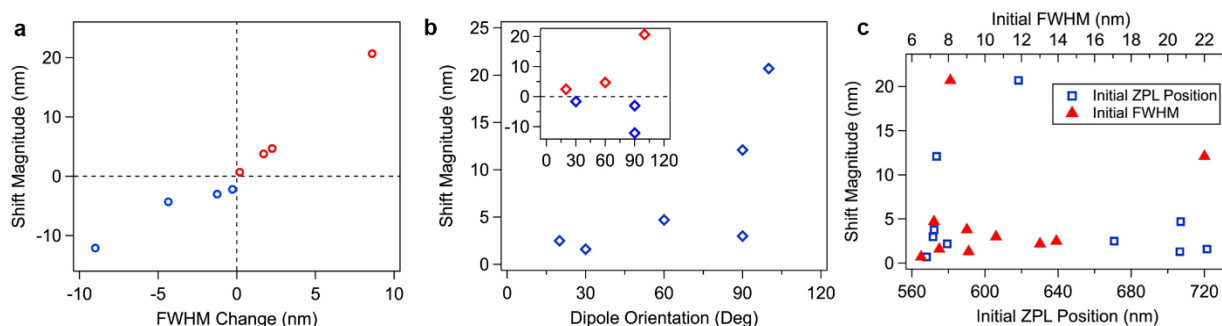


Figure 4: Overall trends of strain modified quantum emission. Each panel displays a plot of the observed shift magnitude vs another independent variable. Each data point represents a different strained quantum emitter. **a.** vs change in the FWHM of the ZPL upon straining, showing each observed shift obeys the red/blue shift rule (i.e. blue shifts decrease e-phonon coupling, while red shifts increase this coupling). **b.** vs the dipole orientation of the unstrained SPE, showing a clear trend towards larger shift magnitudes when the dipole is aligned with the applied strain field. **c.** vs the initial ZPL position (0% strain), showing no observable dependence of shift on initial ZPL spectral position (red triangles). And vs initial FWHM (0% strain), showing no dependence of shift magnitude on the initial peak broadening (blue squares).

Figure 4b displays the observed shift magnitudes as a function of the emission dipole angle, where the strain field is along the 90° axis. As predicted in equation S1, larger shifts are observed when the emission dipole is aligned with the applied strain field. The inset in figure 4b shows that this is the case for both red and blue spectral shifts. Figure 4c, blue boxes, displays the observed spectral shifts as a function of the initial (0% strain) ZPL position. The majority of emitters exhibit a shift of up to ~ 5 nm, however, it was not uncommon to find extremely large spectral shifts exceeding 10 nm.

Figure 4c, red triangles, also plots the shift magnitude relative to the initial peak FWHM, showing no correlation between the magnitude of the spectral shifts and the homogeneous broadening of the SPE. This is an important observation, which suggests that similar shifts should persist even at cryogenic temperatures, where phonon broadening is reduced. This interpretation

is supported by previous results showing up to ~ 9 nm shifts observed upon compressive strain applied through hydrostatic pressure at 20 K.²² To contextualize the degree of shift magnitudes, we consider the largest strain-induced shift to be 10^5 times greater than the expected natural linewidth of the emitter (~ 0.15 μeV linewidth vs ~ 65 meV spectral shift).

In summary, we have demonstrated record tuning magnitudes for a solid-state quantum emitter of up to 65 meV at room temperature. The results were enabled by our newly established technique to grow ultra-thin hBN layers that can be easily transferred to a substrate of choice.²⁹ Importantly, such shift magnitudes help explain the broad and homogeneous distribution of hBN SPEs across the visible spectrum (550-800 nm), and effectively put a lower limit on the influence of strain at ~ 65 meV. Shift direction is determined primarily by a competition between the in-plane strain tensors ϵ_{AC} and ϵ_{ZZ} , while shift magnitude is mediated by the alignment between the defect emission dipole and the applied strain field. We found that blue (red) spectral shifts decrease (increase) the phonon coupling of SPEs and observed that dipole rotation of the SPE towards the applied strain field is possible in some cases. Remarkably, we conclusively proved that all changes are reversible, and the original photophysical properties of the SPEs are restored when the strain field is released.

Our work has several immediate implications in the field of integrated quantum photonics. First, such large shift magnitudes can eliminate hBN defects with inversion symmetry. Such defects are not expected to be amenable to high shifts under applied strain fields.⁷ Therefore, the results support the assignment of the hBN defects in the visible range to defect of the $X_B V_N$ geometry (where X can be a nitrogen or carbon element). Second, our results pave the way for future strain engineering of indistinguishable photons from hBN. Recently, this approach was fruitful to demonstrate indistinguishable photons from silicon-vacancy center (SiV) defects in diamond.^{9, 43} We envision that two or more emitters in hBN can be put in resonance by employing the strain methods using cantilever geometries, as an example.^{8, 44} Third, the technique is fully amenable to the engineering of emitter – cavity coupling, whereby the SPE ZPL can be strain tuned into resonance with the cavity mode.^{10, 45} Finally, and most intriguingly, the strain could be employed to enhance the optically detected magnetic resonance contrast.⁴⁶ The ability to modify the phonon coupling for specific defect transitions provides important control over the system, for instance, controlling the coupling of specific electronic transitions to the surrounding phonon bath has been demonstrated as an effective tool to increase the coherence time of spin-based qubits.^{7, 8} Overall, our work constitutes a significant step forward in understanding light-matter interactions of quantum systems in 2D materials, in their leap towards scalable on-chip devices.

Methods:

hBN Growth and Transfer onto PDMS. The hBN thin-films used in these experiments was fabricated via low-pressure chemical vapor deposition and transferred to the PDMS substrate following an established protocol.²⁹ Briefly, hBN was grown on copper, using ammonia borane as a precursor. Growth was performed at 1030 °C and a pressure of 2 Torr, in a 5% H₂/Ar atmosphere. The as-grown films were then transferred from copper to a PDMS polymer slab via a PMMA assisted wet transfer process. The polymer layer was then removed by soaking the sample in warm acetone (~ 50 °C) overnight, before further cleaning by exposure to UV-Ozone environment for 20 minutes.

Optical Characterization. PL studies were carried out using a home-built scanning confocal microscopy with continuous wave (CW) 532 nm laser (Gem 532, Laser Quantum Ltd.) as excitation. The laser was directed through a 532 nm line filter and a half-waveplate and focused

onto the sample using a high numerical aperture (100×, NA = 0.9, Nikon) objective lens. Scanning was performed using an X–Y piezo fast steering mirror (FSM-300). The collected light was filtered using a 532 nm dichroic mirror (532 nm laser BrightLine, Semrock) and an additional long pass 568 nm filter (Semrock). The signal was then coupled into a graded-index multimode fiber, where the fiber aperture of 62.5 μm serves as a confocal pinhole. A flipping mirror was used to direct the emission to a spectrometer (Acton Spectra Pro, Princeton Instrument Inc.) or two avalanche photodiodes (Excelitas Technologies) in a Hanbury Brown- Twiss configuration, for collection of spectra and photon counting, respectively. Correlation measurements were carried out using a time-correlated single-photon counting module (PicoHarp 300, PicoQuant). All of the second-order autocorrelation $g^2(\tau)$ measurements were analyzed and fitted without background correction unless otherwise specified. For each SPE, ZPL and PSBs were fit with Lorentzian functions to extract both the peak centroid position and the FWHM of the peak.

Acknowledgments

We thank Dr Carlo Bradac and Dr Marcus Doherty for fruitful discussions. The authors thank the Australian Research Council (DP180100070, DP190101058) and the Office of Naval Research Global under grant number N62909-18-1-2025 for financial support.

References:

1. Awschalom, D. D.; Hanson, R.; Wrachtrup, J.; Zhou, B. B., Quantum technologies with optically interfaced solid-state spins. *Nature Photonics* **2018**, *12* (9), 516-527.
2. Atatüre, M.; Englund, D.; Vamivakas, N.; Lee, S.-Y.; Wrachtrup, J., Material platforms for spin-based photonic quantum technologies. *Nature Reviews Materials* **2018**, *3* (5), 38-51.
3. Aharonovich, I.; Englund, D.; Toth, M., Solid-state single-photon emitters. *Nature Photonics* **2016**, *10* (10), 631-641.
4. Wang, J.; Sciarrino, F.; Laing, A.; Thompson, M. G., Integrated photonic quantum technologies. *Nature Photonics* **2019**.
5. Noel H. Wan, T.-J. L., Kevin C. Chen, Michael P. Walsh, Matthew E. Trusheim, Lorenzo De Santis, Eric A. Bersin, Isaac B. Harris, Sara L. Mouradian, Ian R. Christen, Edward S. Bielejec, Dirk Englund, Large-scale integration of near-indistinguishable artificial atoms in hybrid photonic circuits. *arXiv:1911.05265v1* **2019**, *arxiv.org*, e-Print archive <https://arxiv.org/abs/1911.05265> (accessed Nov 18, 2019).
6. Nguyen, C. T.; Sukachev, D. D.; Bhaskar, M. K.; Machielse, B.; Levonian, D. S.; Knall, E. N.; Stroganov, P.; Riedinger, R.; Park, H.; Lončar, M.; Lukin, M. D., Quantum Network Nodes Based on Diamond Qubits with an Efficient Nanophotonic Interface. *Physical Review Letters* **2019**, *123* (18).
7. Meesala, S.; Sohn, Y.-I.; Pingault, B.; Shao, L.; Atikian, H. A.; Holzgrafe, J.; Gündoğan, M.; Stavrakas, C.; Sipahigil, A.; Chia, C.; Evans, R.; Burek, M. J.; Zhang, M.; Wu, L.; Pacheco, J. L.; Abraham, J.; Bielejec, E.; Lukin, M. D.; Atatüre, M.; Lončar, M., Strain engineering of the silicon-vacancy center in diamond. *Physical Review B* **2018**, *97* (20).
8. Sohn, Y. I.; Meesala, S.; Pingault, B.; Atikian, H. A.; Holzgrafe, J.; Gundogan, M.; Stavrakas, C.; Stanley, M. J.; Sipahigil, A.; Choi, J.; Zhang, M.; Pacheco, J. L.; Abraham, J.; Bielejec, E.; Lukin, M. D.; Atature, M.; Loncar, M., Controlling the coherence of a diamond spin qubit through its strain environment. *Nat Commun* **2018**, *9* (1), 2012.

9. Maity, S.; Shao, L.; Sohn, Y.-I.; Meesala, S.; Machielse, B.; Bielejec, E.; Markham, M.; Lončar, M., Spectral Alignment of Single-Photon Emitters in Diamond using Strain Gradient. *Physical Review Applied* **2018**, *10* (2).
10. Elshaari, A. W.; Buyukozer, E.; Zadeh, I. E.; Lettner, T.; Zhao, P.; Scholl, E.; Gyger, S.; Reimer, M. E.; Dalacu, D.; Poole, P. J.; Jons, K. D.; Zwiller, V., Strain-Tunable Quantum Integrated Photonics. *Nano Lett* **2018**, *18* (12), 7969-7976.
11. Konthasinghe, K.; Chakraborty, C.; Mathur, N.; Qiu, L.; Mukherjee, A.; Fuchs, G. D.; Vamivakas, A. N., Rabi oscillations and resonance fluorescence from a single hexagonal boron nitride quantum emitter. *Optica* **2019**, *6* (5).
12. Abidi, I. H.; Mendelson, N.; Tran, T. T.; Tyagi, A.; Zhuang, M.; Weng, L. T.; Özyilmaz, B.; Aharonovich, I.; Toth, M.; Luo, Z., Selective Defect Formation in Hexagonal Boron Nitride. *Advanced Optical Materials* **2019**.
13. Exarhos, A. L.; Hopper, D. A.; Patel, R. N.; Doherty, M. W.; Bassett, L. C., Magnetic-field-dependent quantum emission in hexagonal boron nitride at room temperature. *Nat Commun* **2019**, *10* (1), 222.
14. Bommer, A.; Becher, C., New insights into nonclassical light emission from defects in multi-layer hexagonal boron nitride. *Nanophotonics* **2019**, *0* (0).
15. Vogl, T.; Campbell, G.; Buchler, B. C.; Lu, Y.; Lam, P. K., Fabrication and Deterministic Transfer of High-Quality Quantum Emitters in Hexagonal Boron Nitride. *ACS Photonics* **2018**, *5* (6), 2305-2312.
16. Li, X.; Scully, R. A.; Shayan, K.; Luo, Y.; Strauf, S., Near-Unity Light Collection Efficiency from Quantum Emitters in Boron Nitride by Coupling to Metallo-Dielectric Antennas. *ACS Nano* **2019**, *13* (6), 6992-6997.
17. Nikolay, N.; Mendelson, N.; Özelci, E.; Sontheimer, B.; Böhm, F.; Kewes, G.; Toth, M.; Aharonovich, I.; Benson, O., Direct measurement of quantum efficiency of single-photon emitters in hexagonal boron nitride. *Optica* **2019**, *6* (8).
18. Li, C.; Xu, Z.-Q.; Mendelson, N.; Kianinia, M.; Toth, M.; Aharonovich, I., Purification of single-photon emission from hBN using post-processing treatments. *Nanophotonics* **2019**, *8* (11), 2049-2055.
19. Shevitski, B.; Gilbert, S. M.; Chen, C. T.; Kastl, C.; Barnard, E. S.; Wong, E.; Ogletree, D. F.; Watanabe, K.; Taniguchi, T.; Zettl, A.; Aloni, S., Blue-light-emitting color centers in high-quality hexagonal boron nitride. *Physical Review B* **2019**, *100* (15).
20. Jungwirth, N. R.; Calderon, B.; Ji, Y.; Spencer, M. G.; Flatte, M. E.; Fuchs, G. D., Temperature Dependence of Wavelength Selectable Zero-Phonon Emission from Single Defects in Hexagonal Boron Nitride. *Nano Lett* **2016**, *16* (10), 6052-6057.
21. Tran, T. T.; Elbadawi, C.; Totonjian, D.; Lobo, C. J.; Grosso, G.; Moon, H.; Englund, D. R.; Ford, M. J.; Aharonovich, I.; Toth, M., Robust Multicolor Single Photon Emission from Point Defects in Hexagonal Boron Nitride. *ACS Nano* **2016**, *10* (8), 7331-8.
22. Xue, Y.; Wang, H.; Tan, Q.; Zhang, J.; Yu, T.; Ding, K.; Jiang, D.; Dou, X.; Shi, J. J.; Sun, B. Q., Anomalous Pressure Characteristics of Defects in Hexagonal Boron Nitride Flakes. *ACS Nano* **2018**, *12* (7), 7127-7133.
23. Noh, G.; Choi, D.; Kim, J. H.; Im, D. G.; Kim, Y. H.; Seo, H.; Lee, J., Stark Tuning of Single-Photon Emitters in Hexagonal Boron Nitride. *Nano Lett* **2018**, *18* (8), 4710-4715.
24. Nikolay, N.; Mendelson, N.; Sadzak, N.; Böhm, F.; Tran, T. T.; Sontheimer, B.; Aharonovich, I.; Benson, O., Very Large and Reversible Stark-Shift Tuning of Single Emitters in Layered Hexagonal Boron Nitride. *Physical Review Applied* **2019**, *11* (4).

25. Scavuzzo, A.; Mangel, S.; Park, J.-H.; Lee, S.; Loc Duong, D.; Strelow, C.; Mews, A.; Burghard, M.; Kern, K., Electrically tunable quantum emitters in an ultrathin graphene–hexagonal boron nitride van der Waals heterostructure. *Applied Physics Letters* **2019**, *114* (6).
26. Lazić, S.; Espinha, A.; Pinilla Yanguas, S.; Gibaja, C.; Zamora, F.; Ares, P.; Chhowalla, M.; Paz, W. S.; Burgos, J. J. P.; Hernández-Mínguez, A.; Santos, P. V.; van der Meulen, H. P., Dynamically tuned non-classical light emission from atomic defects in hexagonal boron nitride. *Communications Physics* **2019**, *2* (1).
27. Iikawa, F.; Hernández-Mínguez, A.; Aharonovich, I.; Nakhaie, S.; Liou, Y.-T.; Lopes, J. M. J.; Santos, P. V., Acoustically modulated optical emission of hexagonal boron nitride layers. *Applied Physics Letters* **2019**, *114* (17).
28. Grosso, G.; Moon, H.; Lienhard, B.; Ali, S.; Efetov, D. K.; Furchi, M. M.; Jarillo-Herrero, P.; Ford, M. J.; Aharonovich, I.; Englund, D., Tunable and high-purity room temperature single-photon emission from atomic defects in hexagonal boron nitride. *Nat Commun* **2017**, *8* (1), 705.
29. Mendelson, N.; Xu, Z. Q.; Tran, T. T.; Kianinia, M.; Scott, J.; Bradac, C.; Aharonovich, I.; Toth, M., Engineering and Tuning of Quantum Emitters in Few-Layer Hexagonal Boron Nitride. *ACS Nano* **2019**, *13* (3), 3132-3140.
30. Comtet, J.; Glushkov, E.; Navikas, V.; Feng, J.; Babenko, V.; Hofmann, S.; Watanabe, K.; Taniguchi, T.; Radenovic, A., Wide-Field Spectral Super-Resolution Mapping of Optically Active Defects in Hexagonal Boron Nitride. *Nano Lett* **2019**, *19* (4), 2516-2523.
31. Song, L.; Ci, L.; Lu, H.; Sorokin, P. B.; Jin, C.; Ni, J.; Kvashnin, A. G.; Kvashnin, D. G.; Lou, J.; Yakobson, B. I.; Ajayan, P. M., Large scale growth and characterization of atomic hexagonal boron nitride layers. *Nano Lett* **2010**, *10* (8), 3209-15.
32. Stern, H. L.; Wang, R.; Fan, Y.; Mizuta, R.; Stewart, J. C.; Needham, L. M.; Roberts, T. D.; Wai, R.; Ginsberg, N. S.; Klenerman, D.; Hofmann, S.; Lee, S. F., Spectrally Resolved Photodynamics of Individual Emitters in Large-Area Monolayers of Hexagonal Boron Nitride. *ACS Nano* **2019**, *13* (4), 4538-4547.
33. Wu, F.; Smart, T. J.; Xu, J.; Ping, Y., Carrier recombination mechanism at defects in wide band gap two-dimensional materials from first principles. *Physical Review B* **2019**, *100* (8).
34. Wigger, D.; Schmidt, R.; Del Pozo-Zamudio, O.; Preuß, J. A.; Tonndorf, P.; Schneider, R.; Steeger, P.; Kern, J.; Khodaei, Y.; Sperling, J.; de Vasconcellos, S. M.; Bratschitsch, R.; Kuhn, T., Phonon-assisted emission and absorption of individual color centers in hexagonal boron nitride. *2D Materials* **2019**, *6* (3).
35. Tawfik, S. A.; Ali, S.; Fronzi, M.; Kianinia, M.; Tran, T. T.; Stampfl, C.; Aharonovich, I.; Toth, M.; Ford, M. J., First-principles investigation of quantum emission from hBN defects. *Nanoscale* **2017**, *9* (36), 13575-13582.
36. Wu, F.; Galatas, A.; Sundararaman, R.; Rocca, D.; Ping, Y., First-principles engineering of charged defects for two-dimensional quantum technologies. *Physical Review Materials* **2017**, *1* (7).
37. Gabriele Grosso, H. M., Christopher J. Ciccarino, Johannes Flick, Noah Mendelson, Milos Toth, Igor Aharonovich, Prineha Narang, Dirk R. Englund, Low-temperature electron-phonon interaction of quantum emitters in hexagonal Boron Nitride. *arXiv:1910.02053* **2019**, *arxiv.org*, e-print archive <https://arxiv.org/abs/1910.02053> (accessed Nov 18, 2019).
38. Fu, K. M.; Santori, C.; Barclay, P. E.; Rogers, L. J.; Manson, N. B.; Beausoleil, R. G., Observation of the dynamic Jahn-Teller effect in the excited states of nitrogen-vacancy centers in diamond. *Phys Rev Lett* **2009**, *103* (25), 256404.

39. Plumhof, J. D.; Křápek, V.; Ding, F.; Jöns, K. D.; Hafenbrak, R.; Klenovský, P.; Herklotz, A.; Dörr, K.; Michler, P.; Rastelli, A.; Schmidt, O. G., Strain-induced anticrossing of bright exciton levels in single self-assembled GaAs/Al_xGa_{1-x}As and In_xGa_{1-x}As/GaAs quantum dots. *Physical Review B* **2011**, *83* (12).
40. Martín-Sánchez, J.; Trotta, R.; Mariscal, A.; Serna, R.; Piredda, G.; Stroj, S.; Edlinger, J.; Schimpf, C.; Aberl, J.; Lettner, T.; Wildmann, J.; Huang, H.; Yuan, X.; Ziss, D.; Stangl, J.; Rastelli, A., Strain-tuning of the optical properties of semiconductor nanomaterials by integration onto piezoelectric actuators. *Semiconductor Science and Technology* **2018**, *33* (1).
41. Neu, E.; Agio, M.; Becher, C., Photophysics of single silicon vacancy centers in diamond: implications for single photon emission. *Opt Express* **2012**, *20* (18), 19956-71.
42. Goldman, M. L.; Doherty, M. W.; Sipahigil, A.; Yao, N. Y.; Bennett, S. D.; Manson, N. B.; Kubanek, A.; Lukin, M. D., State-selective intersystem crossing in nitrogen-vacancy centers. *Physical Review B* **2015**, *91* (16).
43. Evans, R. E.; Bhaskar, M. K.; Sukachev, D. D.; Nguyen, C. T.; Sipahigil, A.; Burek, M. J.; Machielse, B.; Zhang, G. H.; Zibrov, A. S.; Bielejec, E.; Park, H.; Loncar, M.; Lukin, M. D., Photon-mediated interactions between quantum emitters in a diamond nanocavity. *Science* **2018**, *362* (6415), 662-665.
44. Kim, H.; Moon, J. S.; Noh, G.; Lee, J.; Kim, J. H., Position and Frequency Control of Strain-Induced Quantum Emitters in WSe₂ Monolayers. *Nano Lett* **2019**.
45. Sipahigil, A.; Evans, R. E.; Sukachev, D. D.; Burek, M. J.; Borregaard, J.; Bhaskar, M. K.; Nguyen, C. T.; Pacheco, J. L.; Atikian, H. A.; Meuwly, C.; Camacho, R. M.; Jelezko, F.; Bielejec, E.; Park, H.; Loncar, M.; Lukin, M. D., An integrated diamond nanophotonics platform for quantum-optical networks. *Science* **2016**, *354* (6314), 847-850.
46. Pingault, B.; Jarausch, D. D.; Hepp, C.; Klintberg, L.; Becker, J. N.; Markham, M.; Becher, C.; Atature, M., Coherent control of the silicon-vacancy spin in diamond. *Nat Commun* **2017**, *8*, 15579.